Joule heating and heat transfer in poly(dimethylsiloxane) microfluidic systems

— Source link ⧉

David Erickson, David Sinton, Dongqing Li

Institutions: University of Toronto

Related papers:

- Temperature measurement in microfluidic systems using a temperature-dependent fluorescent dye.

- Electroosmotic flow with Joule heating effects

- Rapid prototyping of microfluidic systems in poly(dimethylsiloxane)

- Thermal end effects on electroosmotic flow in a capillary

- Joule heating effect on electroosmotic flow and mass species transport in a microcapillary

Joule heating and heat transfer in poly(dimethylsiloxane) microfluidic systems

David Erickson, David Sinton and Dongqing Li*

Department of Mechanical and Industrial Engineering, University of Toronto, 5 King's College Road, Toronto, Ontario, Canada M5S 3G8. E-mail: dli@mie.utoronto.ca

Joule heating is a significant problem in electrokinetically driven microfluidic chips, particularly polymeric systems where low thermal conductivities amplify the difficulty in rejecting this internally generated heat. In this work, a combined experimental (using a microscale thermometry technique) and numerical (using a 3D "whole-chip" finite element model) approach is used to examine Joule heating and heat transfer at a microchannel intersection in poly(dimethylsiloxane) (PDMS), and hybrid PDMS/Glass microfluidic systems. In general the numerical predictions and the experimental results agree quite well (typically within ± 3 °C), both showing dramatic temperature gradients at the intersection. At high potential field strengths a nearly five fold increase in the maximum buffer temperature was observed in the PDMS/PDMS chips over the PDMS/Glass systems. The detailed numerical analysis revealed that the vast majority of steady state heat rejection is through lower substrate of the chip, which was significantly impeded in the former case by the lower thermal conductivity PDMS substrate. The observed higher buffer temperature also lead to a number of significant secondary effects including a near doubling of the volume flow rate. Simple guidelines are proposed for improving polymeric chip design and thereby extend the capabilities of these microfluidic systems.

Introduction

The development of microfluidics-based Lab-on-Chip devices involves the incorporation of many of the necessary components and functionality of a typical laboratory on to a small chip-sized substrate. These integrated, miniaturized systems are stated to offer significant advantages to analytical chemists as they can, in principle, minimize consumption of reagents (by using smaller sample volumes), lessen analysis times, and reduce operating and manufacturing costs.[1–5]

While electrokinetic means can greatly simplify species transport in microfluidic systems, a significant drawback is the internal heat generation (commonly referred to as Joule heating) caused by current flow through the buffer solution. To maintain uniform and controlled buffer temperatures, important for minimizing dispersion in electrokinetic separations[6–7] and inducing temperature sensitive chemical reactions such as DNA hybridization,[8] microfluidic/biochip systems must have the ability to rapidly reject this heat to the surroundings. Generally it is the ability to dissipate this heat that limits the strength of the applied electric field and thus the maximum flow rate.

Recently, microfluidic systems and biochips made from low-cost polymeric materials such as poly(dimethsiloxane) (PDMS),[9–12] poly(methylmethacrylate) (PMMA),[13–15] and others (see Becker and Locascio[16] for a comprehensive review) as opposed to traditional materials such as glass or silicon have become more and more prevalent. The primary attractiveness of these materials is that they tend to involve simpler and significantly less expensive manufacturing techniques (for example: casting, injection and replica moulding, and hot embossing),[16] however they are also amenable to surface modification[17–18] and the wide variety of physiochemical properties allows the matching of specific polymers to particular applications.[9] While the development of these systems has reduced the time from idea to chip from weeks to days, and the per unit cost by a similar ratio (particularly with the advent of rapid prototyping techniques[19]), the low thermal conductivities inherent in these materials (0.18 W m^{-1}K^{-1} for PDMS which

is an order of magnitude lower than that of glass) retards the rejection of internally generated heat during electroosmosis.[16]

A few techniques have been recently developed for making direct "in-channel" measurements of buffer temperatures in microscale systems, the advantages and disadvantages of many of which are discussed in detail by Ross *et al.*[20] While NMR,[21] Raman spectroscopy,[22] and the recently developed on-chip interferometric backscatter detector technique[23] have been used, the most popular techniques involve the addition of temperature sensitive probes (for example: thermochromic liquid crystals,[24] nanocrystals,[25] or special fluorescent dyes[26]) to the buffer solution and an observation of the spatial and temporal changes in the thermal field *via* some type of microscopy technique. Rhodamine B is a fluorescent dye whose quantum yield is strongly dependent on temperature in the range of 0 °C to 100 °C, making it ideal for liquid based systems. Recently Ross *et al.*[20,27] developed a rhodamine B based thermometry technique for monitoring temperature profiles in microfluidic systems, based on that developed by Sakakibara *et al.*[28] for macroscale systems. A similar technique was used by Guijt *et al.*[29] to experimentally examine chemical and physical processes for temperature control in microfluidic systems. In this work we will make use of a rhodamine B based thermometry technique[20] to provide experimental validation and to aid in the development of a detailed numerical model of heat transfer in polymeric and hybrid microfluidic systems.

Computational and analytical modelling has proven to be an excellent tool for analysing electrokinetic flow and transport in microfluidic systems. Primary examples include the works by Ermakov *et al.*,[30] Bianchi *et al.*[31] and Patankar *et al.*[32] who have presented 2D transport models for several microfluidic processes. Recently both Molho *et al.*[33] and Griffiths and Nilson[34] have used combined analytical and numerical approaches to study band spreading and to optimise turn geometries in microfluidic systems. In one of the first 3D analyses of electrokinetic flow, Erickson and Li[35] used finite element simulations to examine the effects of surface heterogeneity on the mixing efficiency at a T intersection. In terms of thermal analysis a few recent studies have examined, either experimen-

tally or analytically, heat transfer processes using electro-osmotic flows,[36–38] however these have focused primarily on enhancing heat transfer from integrated circuits and detailed examinations of the flow field using idealized boundary conditions. In general very little work has been done concerning microscale thermal analysis as related to microfluidic based biochips on a "whole-chip" basis (as opposed to examining just the fluidic domain for example), particularly with respect to the recently developed polymeric systems.

In this work we present a detailed experimental and numerical analysis of the dynamic changes in the in-channel temperature and flow profiles during electrokinetic pumping at a T-shaped microchannel intersection, using pure PDMS/PDMS and PDMS/Glass hybrid microfluidic systems. A T-intersection was selected for this study as it represents the most general intersection of a microfluidic system and it provides an interesting theoretical case due to the inherent spatial gradients in current density and volumetric flow rate. Using a fluorescence based thermometry technique, direct measurements of the in-channel temperature profile are taken and the results compared with a detailed "whole-chip" finite element model, which accounts for the effects of the temperature field on the local solution conductivity and fluid viscosity as well as thermal conduction through the substrate. The modeling developed here addresses the need, as discussed by Swinney and Bornhop,[23] to revisit some simple earlier models of on-chip heat rejection (such as that by Jannson et al.[39]) in light of: disagreements with experimental results obtained with newly developed microscale thermometry techniques,[23] the growing popularity of polymeric and hybrid microchannel constructions,[16] and the increasing complexity of microchannel networks. The analysis examines, for the first time, the primary mechanisms whereby heat is rejected initially from the buffer solution to the substrate and then from the substrate to the environment. The results are then exploited to propose novel ways of both enhancing and controlling on-chip heat transfer, thereby extending the capabilities of polymeric microfluidic systems.

Theory

Thermal analysis and simulation domain

Unlike momentum and species transport analysis, which is confined to the fluidic domain, thermal modelling in microfluidics presents some unique challenges as the presence of thermal diffusion necessarily extends the simulation domain from the region of interest (i.e. the fluidic domain) to encompass a significant portion of the chip, if not the entire chip. Different from a macroscale system, where the fluidic domain is most often of comparable size to the solid regions, a microchannel system typically encompasses only a very small fraction of the substrate and thus heat transfer is typically governed by a large timescale thermal diffusion process through the solid region. As is shown in Fig. 1, the system of interest here comprises three coupled domains, the lower substrate (made from either glass or PDMS), fluidic domain (buffer solution) and the upper substrate which contains the channel pattern (made from PDMS).

Electroosmotic flow occurs when an applied driving voltage interacts with the charge in the electrical double layer near the liquid/solid interface resulting in a local net body force that tends to induce bulk fluid motion. When this voltage is applied to a buffer solution with a finite conductivity, the resulting current induces an internal heat generation effect often referred to as Joule heating. Within the fluidic domain the non-dimensional energy equation takes the form,

$$Pe_{F}\left[\frac{\partial\theta}{\partial\delta}+V\tilde{\nabla}\theta\right]=\tilde{\nabla}^2\theta+\Lambda\left|\tilde{\nabla}\Phi\right| \quad (1)$$

where Pe_{F} is the Péclet number for the fluidic domain ($Pe = \rho C_p L v_o/k$ where ρ is the density, C_p is the specific heat, L is a length scale taken to be the channel height in this case, v_o is the reference velocity and k is the thermal conductivity), θ is the non-dimensional temperature ($\theta = (T-T_o)k_L/\lambda_o\phi^2_{max}$ where λ_o is the electrical conductivity at the reference temperature, T_o, ϕ_{max} is the maximum applied voltage and the subscript L signifies properties of the liquid domain), d is the non-dimensional time, V is the non-dimensional velocity ($V = v/v_o$) which will be obtained via the fluidic analysis discussed below, Λ, is the non-dimensional buffer electrical conductivity ($\Lambda = \lambda/\lambda_o$) and is in general a function of temperature, Φ is the non-dimensional applied electric field strength ($\Phi = \phi/\phi_{max}$), and the ~ symbol over the ∇ operator indicates the gradient with respect to the non-dimensional coordinates ($X = x/L$, $Y = y/L$ and $Z = z/L$). While most thermal properties in the above formulation (i.e. C_p, k, etc.) remain relatively constant over the temperature range of interest,[40] and thus have been assumed so for the purposes of this study, the buffer electrical conductivity has a strong temperature dependence which cannot be ignored. Here we assume that the buffer conductivity is linearly proportional to temperature (having slope α) as shown in eqn. (2),

$$\Lambda = \lambda/\lambda_o = 1 + \alpha\theta \quad (2)$$

Within the upper substrate (subscript US) and lower substrate (subscript LS) the energy equation takes on a simplified form in that convective effects and the internal heat generation term is absent leaving only the transient and diffusion terms as shown below,

$$Pe_{LS,US}\left[\frac{\partial\theta}{\partial\delta}\right]=\nabla^2\theta \quad (3)$$

As mentioned above, the dominant mechanism of heat rejection from the fluidic domain is diffusion into the solid substrate. For very short times the temperature field is confined to a small region around the channel. However, at longer times (approaching those which are required for the system to reach equilibrium) the temperature field can span an area several orders of magnitude larger than the channel size, due to lateral thermal diffusion. This poses significant computational problems as it introduces another length scale into the problem. While the height of the computational domain is fixed by the
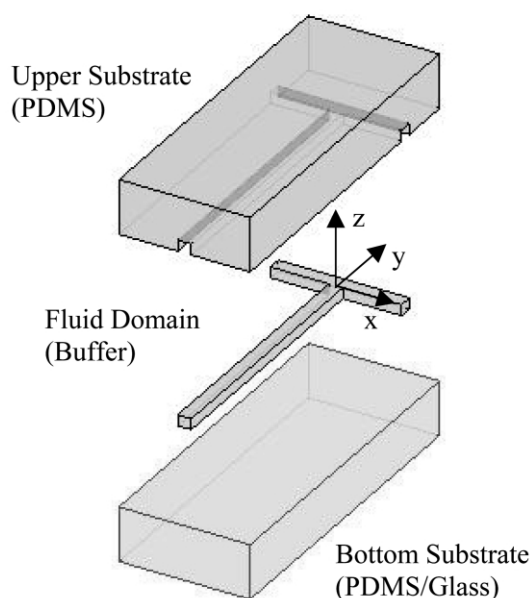

Fig. 1 Computational geometry for PDMS/PDMS or PDMS/Glass hybrid microfluidic system.

system geometry, the required width of the domain was found to be approximately 50 times the channel width through numerical experimentation. Choosing a smaller domain necessarily led to a significant underestimation of the lateral heat transfer. Boundary conditions on the thermal domain were selected to conform with how most chip based microfluidic experiments are conducted. The lower surface of the substrate was assumed to be fixed at the room temperature (as would be the case for a chip sitting on a relatively large flat surface) while the upper surface was assigned a free convection boundary condition,

$$\frac{\partial \theta}{\partial Z} + Bi\theta = 0 \tag{4}$$

where Bi is the Biot number ($Bi = hL/k_{US}$ where h is the heat transfer coefficient computed from the "heated upper plate" relation from Incropera and DeWitt[40] to be $h = 10\ \mathrm{W\ m^{-2}K^{-1}}$). Zero flux conditions were used along the side surfaces.

Fluidic analysis

In general the high voltage requirements limit most practical electroosmotically driven flows in microchannels to small Reynolds numbers therefore transient and momentum convection terms in the Navier-Stokes equations can be ignored[41] and thus the fluid motion is governed by the Stokes, eqn. (5), and continuity, eqn. (6), equations as shown below,

$$-\tilde{\nabla}P + \tilde{\nabla}\sigma + \left(\frac{\varepsilon_w \phi_{\max} k_b T}{ze\eta_o v_o L}\right)\left[\tilde{\nabla}^2\Psi\ \tilde{\nabla}\Phi\right] = 0 \tag{5}$$

$$\tilde{\nabla}V = 0 \tag{6}$$

where σ is the non-dimensional shear stress ($\sigma = \tau/(\eta_o v_o/L)$, where τ is the fluidic shear stress[41] and η_o is the viscosity at a reference temperature, P is the non-dimensional pressure, Ψ represents the non-dimensional EDL field strength ($\Psi = z\psi e/k_b T$, where k_b is the Boltzmann constant, T is the absolute temperature, e is the charge of an electron, and z is the ionic valence), and ε_w is the electrical permittivity of the solution.

As is discussed in detail by Erickson and Li,[35] numerical modeling of electroosmotic flow is complicated by the simultaneous presence of three separate length scales; the channel length (mm), the channel depth or width (μm) and the double layer thickness (nm). The simplest way to alleviate this problem is to apply a slip boundary condition at the channel wall ($V_{\mathrm{wall}} = \mu_{eo}\nabla\phi/v_o$ where $\mu_{eo} = \varepsilon_w \zeta/\eta$ is the electroosmotic mobility and z is the zeta potential) and solve for the bulk fluid motion. Since $\Psi = 0$ within the bulk fluid this eliminates the forcing term in eqn. (1) and thus the double layer field from the formulation. As is well known, and was directly observed recently by Ross et al.,[42] μ_{eo} tends to increase with temperature mostly due to its inverse relationship with viscosity. As with electrical conductivity, the temperature dependence of viscosity is too significant to be ignored and thus we model the changes in viscosity using the following relationship,[43]

$$\ln\frac{\eta}{\eta_o} = -1.704 - 5.306\left(\frac{273}{T}\right) + 7.003\left(\frac{273}{T}\right)^2 \tag{7}$$

where η_o is the viscosity at 0 °C ($1.788 \times 10^{-3}\ \mathrm{kg\ m^{-1}s^{-1}}$).

The potential field, required as part of the internal heat generation term in eqn. (1) and for the boundary condition on eqn. (6) and again solved within the fluidic domain, is described by eqn. (8),

$$\tilde{\nabla}\left(\Lambda\tilde{\nabla}\Phi\right) = 0 \tag{8}$$

which varies from the traditional Laplace equation[35] in that the temperature dependence of conductivity has been accounted

for. Insulation boundary conditions are assigned along the edges of the domain while fixed conditions are applied at the upstream inlets ($\Phi = 1$) and downstream outlets ($\Phi = 0$).

Numerical technique

The above sets of equations have been solved using an in-house written finite element code. The code discretizes the computational domain using 27-noded 3D brick elements and makes use of tri-quadratic basis functions for integration of the unknowns. The coupled Navier-Stokes and continuity equations were solved using a penalty method approach, which eliminates the pressure variable from the formulation. The transient convection diffusion problems associated with the thermal analysis were discretized using an implicit first order Euler scheme and solved using an iterative bi-conditioned stabilized conjugate gradient method. As discussed above both the velocity and potential fields are strongly dependent on the changes in the temperature field and thus need to be updated periodically. In the solution scheme used here both these fields were updated every 1 s (or approximately every 5 time steps) which was found to be a good compromise between solution accuracy and computational time.

Experimental

Chemicals and materials

Laser grade rhodamine B dye (Acros Organics, Pittsburgh, Pennsylvania) was initially dissolved in pure water at a concentration of 1 mM and stored at −30 °C. Prior to the experiments the dye was further diluted to a concentration of 50 μM in 25 mM carbonate buffer solution at a pH of 9.4. All solutions were filtered before use with a 0.2 μm syringe filter (Whatman, Ann Arbor, Michigan).

SU-8–25 photoresist (Microchem, Newton, Massachusetts) and Diacetone-alcohol developer solution (Sigma-Aldrich, St. Louis, Missouri) were used in the making of the positive relief masters by the procedure outlined below. PDMS casts were prepared by thoroughly mixing the base and curing agent at a 10:1 ratio as per the manufacturers instructions for the Sylgard 184 silicon elastomer kit (Dow Corning, Midland, Michigan). Caution was used to avoid contact between the liquid PDMS and latex rubber (gloves) as this was found to inhibit curing.

Microchannel fabrication

The PDMS/PDMS and hybrid PDMS/Glass microchannel systems used here were manufactured using the soft lithography technique developed by Duffy et al.[19] Briefly, masters containing the desired microchannel pattern were made by spin coating SU-8 negative photoresist on a glass slide to a nominal thickness of 20 μm. The photoresist film was then hardened through a two stage direct contact pre-exposure bake procedure (65 °C for 5 min and 95 °C for 15 min) and exposed to UV light for 2.5 min through a 3500 dpi transparency mask (Screaming Colors, Edmonton, Alberta) containing the desired channel pattern. A two stage post-exposure bake procedure (65 °C for 1 min 95 °C for 2 min) was then used to enhance cross-linking in the exposed portion of the film. The slide was then placed in quiescent developer solution for 10 min to dissolve the unexposed photoresist, leaving a positive relief containing the microchannel pattern.

Liquid PDMS was then poured over the master and cured at 65 °C for 6 to 12 h yielding a negative cast of the microchannel pattern. An enclosed microchannel was then formed by bonding the PDMS cast with either another piece of PDMS or a glass

slide (forming the lower substrate) by placing both sides in a plasma cleaner (PDC-32G, Harrick Scientific, Ossining, New York) and oxidizing them for 45 s. This was done immediately after removal of the PDMS cast from the master to minimize surface ageing effects as described by Ren *et al.*[44] When glass slides were used as the lower substrate, they were initially soaked in acetone overnight, rinsed in DIUF (Deionised Ultra Filtered) water and then dried at 200 °C to remove any excess water prior to being placed in the plasma cleaner. Following oxidation the two halves were brought into contact and an irreversible seal was formed. After sealing carbonate buffer solution was introduced into the channels by applying a negative pressure at the downstream end.

Experimental technique and image analysis

Rhodamine B dye is one of a class of fluorescent dyes whose quantum yield is strongly dependent on temperature.[26] As such the in-channel temperature profile can be obtained by observing the relative spatial and temporal changes in the local intensity of the dye using a fluorescence imaging technique similar to that developed by Ross *et al.*[20] In our experiment a Leica DM-LB fluorescence microscope (Leica Microsystems (Canada), Richmond Hill, Ontario) with a 10×, 0.3 N.A. long working distance objective, a rhodamine B filter set (excitation: band pass 546 nm/12 nm, emission: band pass 600 nm/40 nm) and a broadband mercury illumination source was used. 12-bit, 1024 × 1280 pixel greyscale intensity images were captured every 0.25 s for approximately 40 s using a Retiga-1300 cooled digital CCD camera (Qimaging, Burnaby, British Columbia) at a typical exposure time of 10 ms. Image acquisition and storage was controlled by Openlab software (Improvision, Guelph, Ontario).

Prior to each experiment the microchannel system was allowed to cool to room temperature and an isothermal "cold field" intensity image of the system was taken. Following the acquisition of the cold field image, the electric field was switched on (inducing electroosmotic flow and joule heating in the microchannel) and full speed image acquisition was initiated. In all cases a uniform potential was applied at all upstream inlet reservoirs while the downstream waste reservoir was grounded. Current/Voltage monitoring was done through dual 0–10 V signals, output from the high voltage source (Spellman, Hauppauge, New York), and captured using a data acquisition card and a custom designed software interface. Following the capture of 150 high resolution images the excitation light was blocked and the electric field was turned off, allowing the system to cool back down to room temperature. After cooling was complete a second cold field image was acquired. The second cold field image was then compared to initial image and in general it was found that the intensity values of the two images were identical, suggesting that any photobleaching of the dye during the experiment was not significant.

To extract the in-channel temperature profiles from the captured intensity images each was first normalized by the cold field image as described above. A Wiener type adaptive filter was then applied in order to smooth the images and reduce the effect of any background noise. The intensity values of treated images were then converted to temperature using the intensity *vs.* temperature calibration discussed in the proceeding section.

Temperature dependent dye calibration

To calibrate the intensity *vs.* temperature behavior of the dye, a PDMS vessel, containing approximately 1 mL rhodamine B dye solution, with two embedded type-J thermocouples was con-

structed. Initially the vessel was loaded with dye solution at room temperature and the entire system was heated to approximately 80 °C. The system was allowed to cool in air while intensity images were taken at specified intervals and the data acquisition system recorded the instantaneous thermocouple readings. The low thermal conductivity of the PDMS vessel ensured a uniform temperature profile within the higher thermal conductivity liquid region. Random locations in the calibration images were then selected and the intensities at each point were scaled by the cold field image at 30 °C (a 30 °C cold field image was used here since below that the error in the thermocouple measurement became significant compared with the temperature difference). The data was then normalized such that an intensity of 1 corresponded to room temperature. The final results are shown in Fig. 2. When compared, these results were found to compare very well (within ± 1 °C) with those presented by Ross *et al.*[20] for similar buffer concentration and pH.

Results and discussion

As described above, electrokinetic pumping can greatly simplify species transport in microfluidic systems, however Joule heating caused by the current flow through the liquid can lead to significant increases in the buffer temperature. Recently, largely due to their low cost and ease of manufacture, polymer based microfluidic systems have become more and more popular. These polymers typically posses low thermal conductivities which amplifies the difficulty in rejecting this internally generated heat. Here we study this using independent experimental (using a temperature sensitive fluorescent probe) and numerical (using finite element simulations) approaches.

The T-shaped microchannel intersection used in this study is illustrated in Fig. 1. The two inlet channels have a width of 100 μm and a length of 6 mm, the single outlet channel has a 120 μm width and is 24 mm long, and all channels are 20 μm deep. In Figs 3 and 4 we consider two construction configurations, a PDMS/PDMS system (where both substrates are composed of PDMS, Fig. 3) and a PDMS/Glass hybrid system (where the bottom substrate is glass and the upper substrate is PDMS, Fig. 4). For both cases the thickness of the upper PDMS piece (containing the channel design) was 1.0 mm, while the lower substrate for the PDMS/PDMS chip was 1.75 mm and 1.0 mm for the PDMS/Glass chip. In each case a potential of 2.05 kV was applied to the inlet reservoirs and the downstream outlet was grounded. Thermophysical properties of materials used in the chip construction are shown in Table 1. The buffer
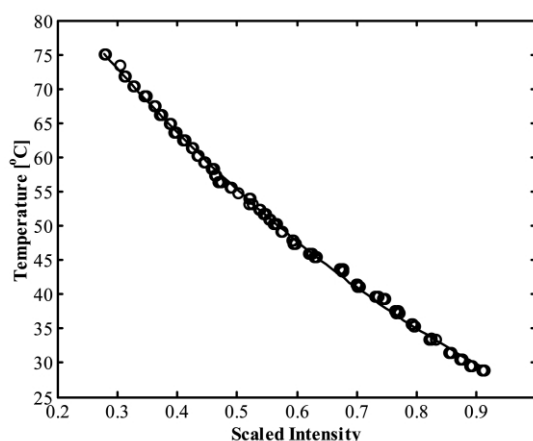

Fig. 2 Measured temperature as a function of scaled fluorescence intensity of rhodamine B dye. Solid line represents a second order polynomial fit to the data.
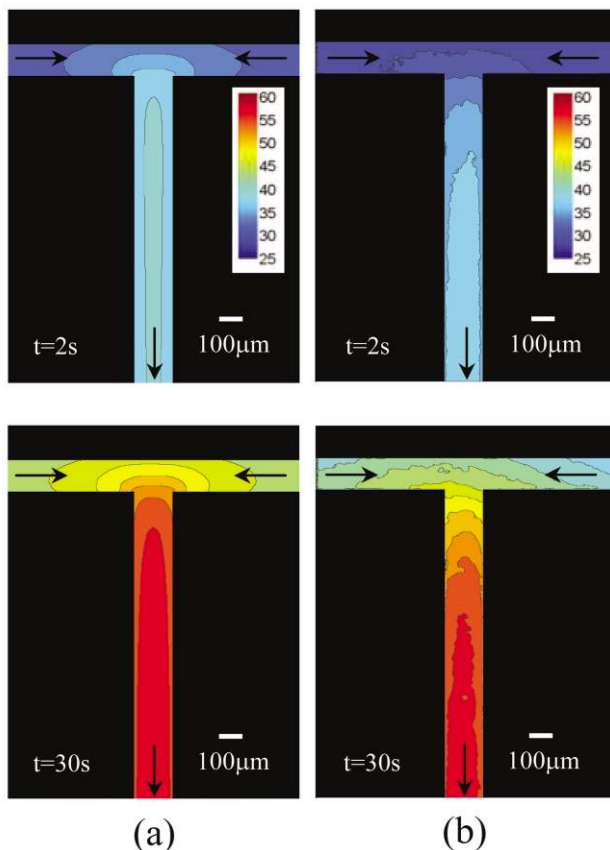
Fig. 3 Comparison between numerically (a) and experimentally (b) obtained temperature profiles in a T intersection for the PDMS/PDMS chip. A 2.05 kV electric field strength was applied.
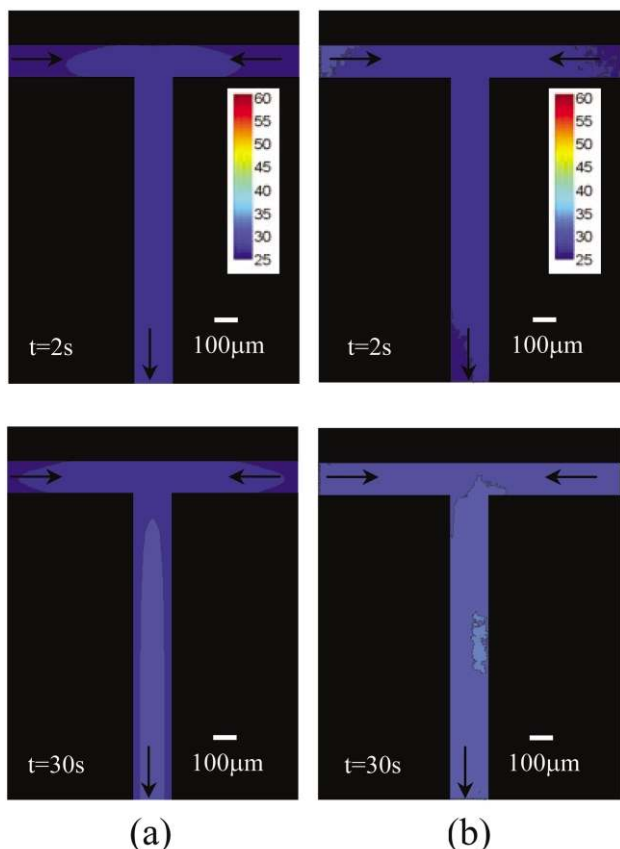

Fig. 4 Comparison between numerically (a) and experimentally (b) obtained temperature profiles in a *T* intersection for a PDMS/Glass hybrid chip. A 2.05 kV electric field strength was applied.

conductivity at 25 °C was measured as 0.22 $\Omega^{-1}m^{-1}$ and was found to increase approximately 3%/°C (this relationship was used in determining a from eqn. (2)). μ_{eo} for the PDMS/PDMS and PDMS/Glass systems were taken as 6.2×10^{-4} cm² $V^{-1}s^{-1}$ and 6.0×10^{-4} cm² V^{-1} s⁻¹ respectively.[42]

Thermal analysis

Prior to examining the results it is useful to compare the numerical and experimental predictions. As can be seen in Figs 3 and 4, the experimental and numerical in general agree quite well, typically within ±3 °C, with the numerical predictions tending to slightly overestimate the temperature profile. The likely cause of the overestimation are the unknowns in the thermal properties of PDMS for which only approximate values could be obtained.[45] The average noise level in the experimental results was approximately ±1 °C, which was reduced through the smoothing procedure discussed above, and the observed repeatability was approximately ±2 °C. The slight asymmetry in the experimental temperature profiles may have been caused by slight structural irregularities at the channel/reservoir interface, created during the reservoir cutting process, or a non-uniform channel depth, as a result of the photoresist spin coating process. The experimental results shown in Figs 3 and 4 represent the median case of all experiments preformed.

Immediately apparent by comparing either the numerical or experimental results is the dramatic difference between the temperature rise observed in the PDMS/PDMS system compared with the PDMS/Glass system. As can be seen, after 30 s the PDMS/PDMS system obtained a maximum temperature in the mixing channel of 58 °C while at the same point the hybrid system reached only 32 °C. This suggests that indeed the much higher thermal conductivity of the glass substrate (1.4 W mK⁻¹ as opposed to 0.18 W mK⁻¹ for PDMS) does significantly improve the heat transfer qualities of the microfluidic system. To analyse the primary cooling mechanisms involved in this effect, consider the dominant heat transfer mechanism on two different timescales. In the initial heating stages, the primary fluid cooling mechanism is the transient but relatively slow heating of the surrounding substrate. During these times an exponential rise in the temperature profile can be expected (*i.e.* behaviour consistent with a semi-infinite solid[40]), as was observed by Ross *et al.*[20] Beyond this initial substrate heating stage (*i.e.* at times approaching those required to reach a steady state) the system temperature is governed by the rate of heat rejection from the substrate to the surroundings. To examine this consider Fig. 5 which shows the computed temperature contours within the solid substrates and the fluidic region, after the 2.05 kV potential has been applied for 30 s, for the identical (a) PDMS/PDMS and (b) PDMS/Glass systems discussed above. As can be seen for the PDMS/PDMS system, the temperature profile in the substrate is centered around the fluid region and then spreads radially outwards. The obvious temperature gradients seen here demonstrate the inapplicability of earlier on chip heat rejection models, which assume isothermal conditions,[39] to polymeric substrates. As we get farther away from the fluidic region, boundary effects begin to influence the temperature profile and it can be noted that the temperature gradients become sharper in the lower substrate

Table 1 Thermophysiscal properties of chip materials

	Thermal conductivity, k/ W m⁻¹K⁻¹	Specific heat, C_p/ J kg⁻¹K⁻¹	Density, ρ/ kg m⁻³
PDMS[45]	0.18	1100	1030
Glass[40]	1.4	835	2225
Buffer[40]	0.61	4179	1030

than in the upper. The sharper gradients suggest that at these longer times the majority of the heat transfer is rejected through the lower substrate to the room temperature reservoir on the underside of the chip (despite the larger thickness of the lower substrate) as opposed to free convection from the upper surface.

We can examine this effect in greater detail by considering a simple steady state thermal resistance model of heat transfer through the upper and lower substrates in eqns. (9a) and (9b) below,

$$R_{LS} \propto \frac{l_{LS}}{k_{LS}} \qquad (9a)$$

$$R_{US} \propto \left(\frac{l_{US}}{k_{US}} + \frac{1}{h} \right) \qquad (9b)$$

where R is the resistance to heat transfer and l is the thickness of the substrate.[40] It is important to note here that these equations ignore lateral heat transfer and transient effects and thus cannot be used to make direct predictions of the channel temperature (hence the need for the complex 3D numerical model). As is discussed below, they do however allow for order of magnitude estimates of how chip design changes will affect the heat transfer properties of a microfluidic system. For the PDMS/PDMS system then the RLS:RUS ratio is approximately 0.09 suggesting that over 10 times as much heat is transferred through the lower substrate to the room temperature reservoir than through the upper substrate. This has significant implications for the design of PDMS microsystems in that the effects of Joule heating can be dramatically reduced by (eqn. (9a)) either reducing the thickness of the lower substrate or increasing its thermal conductivity. The coupling of these effects are shown in Fig. 5b (PDMS/Glass system) where the smaller lower substrate thickness and higher thermal conductivity has greatly improved the chips ability to regulate the buffer temperature. The upper substrate thickness and material properties are considerably less important since the thermal resistance (from eqn. (9b)) is dominated by the convective heat transfer term (i.e. $1/h$). Thus significant enhanced heat transfer through the upper substrate can only be obtained by incorporating forced convection or enhanced heat transfer surface (e.g. fins).

In both cases shown in Fig. 3 and Fig. 4 a significant change in the buffer temperature is observed as the two inlet channels converge into the single outlet channel, similar to that observed by Ross et al.[20] in acrylic microchannels, due to differences in the rate of internal heat generation in the inlet channels, where both the current and potential field gradient are approximately half that of the mixing channel. It was proposed in that work that such constrictions could be used as a technique for inducing temperature dependent chemical reactions. As can be seen in Fig. 4, these gradients tend to be smoothed out by the presence of the glass lower substrate, due to the lower lateral thermal resistance. As such, while a hybrid system is much more effective at maintaining a constant buffer temperature, the pure PDMS system is more effective at maintaining on-chip temperature differences (such as those that would be required for the aforementioned thermal cycling technique).

The influence of the electric field strength on the temperature rise is demonstrated in Fig. 6 which shows the temperature profile along the centreline of the mixing channel for the PDMS/PDMS system, 30 s after the potential field was turned on. As expected the decrease in the potential field leads to a significantly lower buffer temperature, however we also note a slightly more uniform temperature field near the intersection. This is a result of the reduction in the magnitude of the convective term in eqn. (1), which tends to push the colder liquid in the inlet arms into the mixing channel, since the lower applied electric field also reduces the magnitude of the electroosmotic velocity.
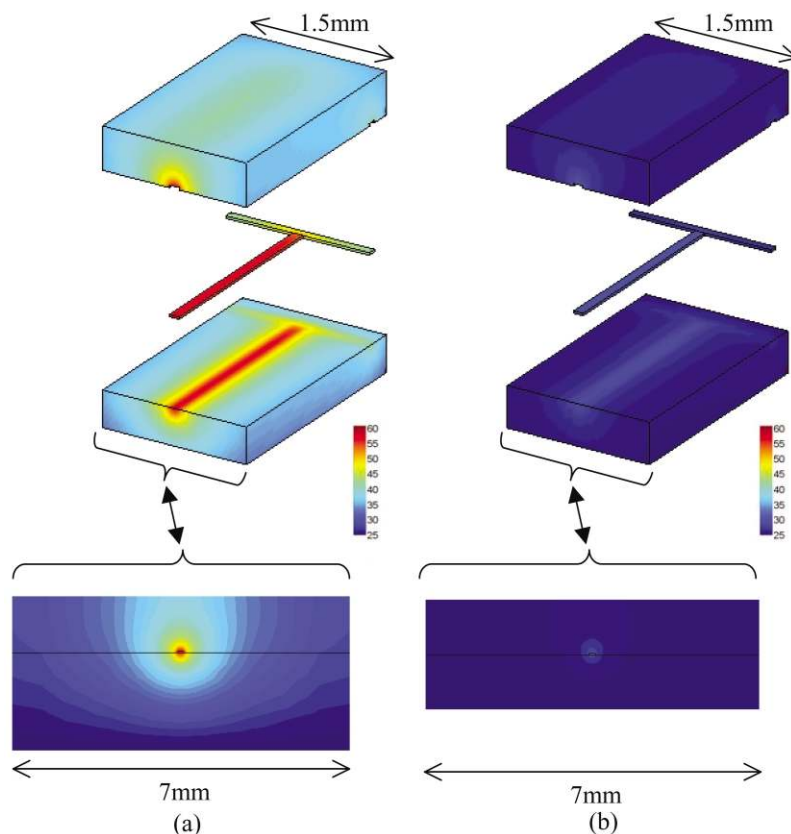

Fig. 5 Simulated temperature contours for the (a) PDMS/PDMS and (b) PDMS/Glass composite systems 30 s after a 2050 kV voltage was applied (identical to cases shown in Figs 3 and 4). Upper image shows the 3D temperature contours in the substrates in the region very near the fluidic region while lower figure details the 2D temperature profile 2.5 mm downstream of the intersection. Entire computational domain not shown.

It is also informative to examine the current load on the system for the two cases. Fig. 7 compares both the experimentally measured and numerically calculated total current draw through the two systems discussed above. As before we see good agreement between the experimental and numerical predictions, with the numerical results tending to slightly underestimate the current, but exhibiting a similar trend. Of interest here is the dramatic difference between the current draw between the PDMS/PDMS and PDMS/Glass system, which can be attributed to the increase in solution conductivity with temperature. Fig. 8 compares the non-dimensional conductivity, Λ, at the midplane of the channel 30 s after the 2.05 kV potential has been applied for the (a) PDMS/PDMS and (b) PDMS/Glass systems discussed above. As expected a dramatic change in the conductivity profile is observed near the intersection (corresponding to the sharp temperature gradients also observed there) nearly doubling the buffer conductivity in the mixing channel after 30 s while the PDMS/Glass systems maintains a much more uniform conductivity. Such rapid changes in the solution conductivity can have dramatic effects on the local potential field, *via* eqn. (8), and thus are very important in, for example, sample transport. These local Joule heating induced conductivity differences present an interesting alternative to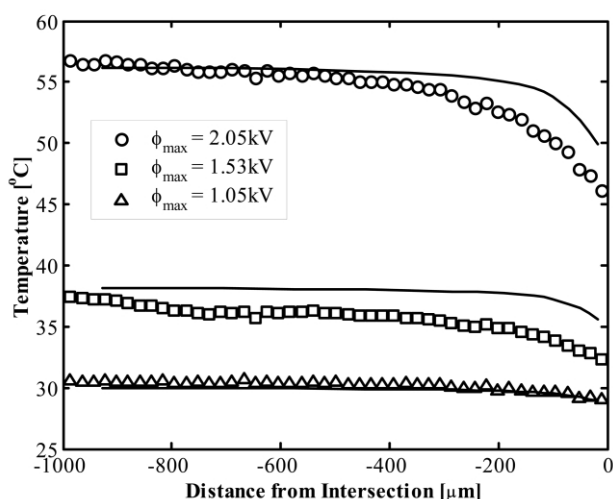 concentration induced conductivity differences employed previously to mitigate (pumping) or induce (stacking) separation effects.[46–47] This increasing of the electrical conductivity necessarily results in an increase in the rate of internal heat generation which, as can be seen in Fig. 7, results in the continual increase in the current load for the PDMS/PDMS system whereas the hybrid system tends to level off much sooner. This continual increase is reflective of the fact that the large substrate to fluid ratio coupled with this temperature dependent conductivity, significantly increases the time required to reach a steady state.

Fluidic analysis

As mentioned above the electroosmotic mobility tends to increase with temperature primarily due to its inverse relationship with viscosity. As such it is of interest here to examine how significantly the system flow rate will be affected by the joule heating discussed earlier. Fig 9 compares the computed volume flow rate (*i.e.* in the mixing channel) 30 s after the voltage has been applied for the two cases shown in Figs 3 and 4. As can be seen despite having nearly identical electroosmotic motilities at room temperature (6.2×10^{-4} cm^2 V^{-1} s^{-1} for the PDMS/ PDMS and 6.0×10^{-4} cm^2 V^{-1} s^{-1} PDMS/Glass,[42] as

Fig. 6 Effect of applied potential field strength on the temperature profile in the mixing channel of the PDMS/PDMS system 30 s after the indicated potential has been applied. Hollow markers represent experimental results and solid lines show numerical predictions.
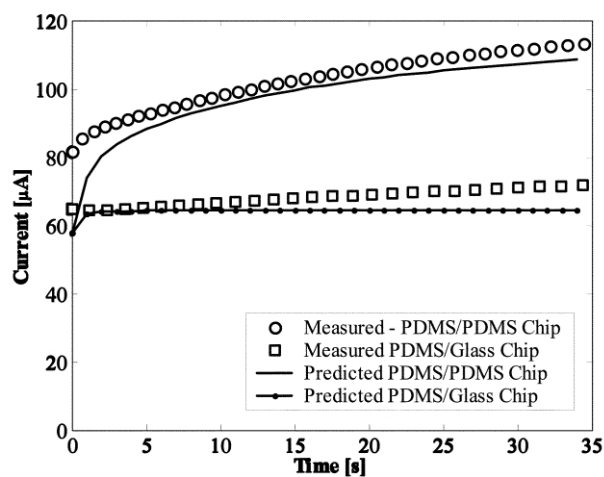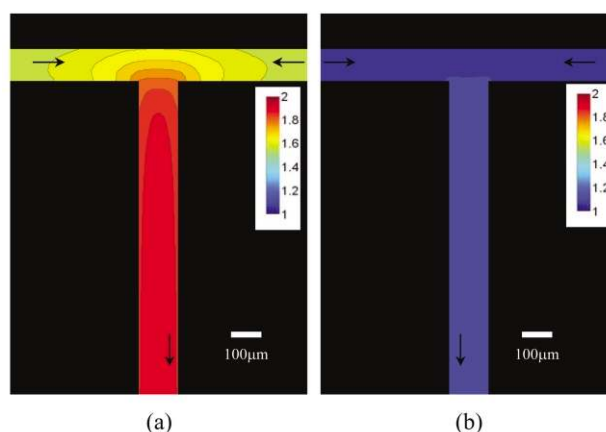

Fig. 8 Computed non-dimensional conductivity profiles in the (a) PDMS/ PDMS system and (b) PDMS/Glass system after a 2.05 kV voltage has been applied for 30 s. Conditions are identical to those discussed for the experiments shown in Figs 3 and 4.
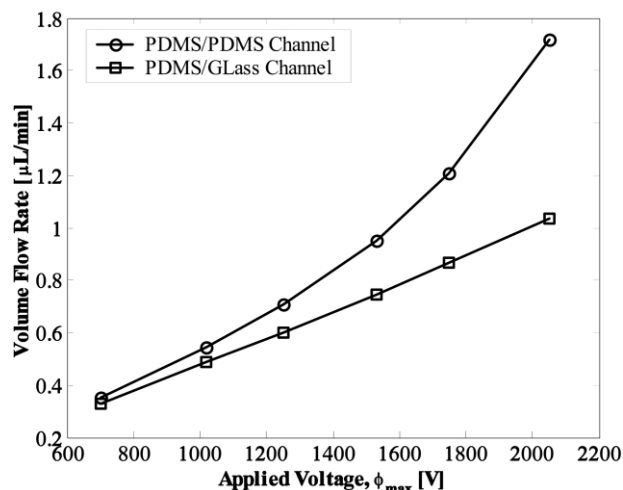

Fig. 7 Comparison between experimentally measured and numerically predicted current load for the experiments shown in Figs 3 and 4. In all cases a 2.05 kV electric field strength was applied. For clarity not all experimental data points are shown.

Fig. 9 Computed volume flow rate in mixing channel for PDMS/PDMS and PDMS/Glass system 30 s after the voltage is applied. Conditions similar to those for results shown in Figs 3 and 4.

mentioned earlier) the higher temperature rise in the PDMS/PDMS system significantly increases the volume flow rate over that in the PDMS/Glass system. This could be of substantial importance when attempting to deliver precise quantities of reactants for downstream separation or chemical reactions. Fig. 10 examines in more detail the flow field at the channel midplane 30 s after the potential is applied for the 2.05 kV case. As discussed, the velocity vectors are significantly larger in the PDMS/PDMS system, however despite the relatively large changes in the local temperature (and thus viscosity) the flow structure and velocity profile do not change greatly. In the mixing channel, where the temperature is the highest, the viscosity is the lowest (tending to induce a higher velocity) however the higher conductivity tends to reduce the potential field gradient (tending to induce a lower velocity). As a result the viscosity and potential fields tend to have a somewhat counterbalancing effect which tends to maintain the overall flow structure.

Influence of channel aspect ratio

Before finishing it is of interest to examine how the channel aspect ratio can influence the temperature profile in the channel. In general it is relatively well understood that microchannels with a larger surface area to volume ratio are better at rejecting internally generated heat to the substrate (see Swinney and Bornhop[23] for a brief discussion) but it is of interest here to quantify how significant this effect will be in low thermal conductivity polymeric substrates. Fig. 11 shows the mixing channel temperature profile for the PDMS/PDMS system, shown in Fig. 3, 30 s after the 2.05 kV potential is applied. In all cases the channels have a cross sectional area of 3600 μm^2 such that the rate of internal heat generation and current load in the initially isothermal system were equivalent. As expected the buffer temperatures remained lowest for the very large aspect ratios (25% lower for W/H = 36 vs. W/H = 1). Such large aspect ratios however pose significant operational and construction difficulties (particularly for soft elastomers like PDMS which tend to sag in the middle of such wide, thin channels). For more practical aspect ratios however (W/H = 2 for example) it can be seen that the computed temperature difference is < 1 °C and thus is not particularly significant.

Conclusions

Electrokinetic pumping can greatly simplify species transport in microfluidic systems, however Joule heating caused by the current flow through the buffer solution can lead to significant increases in the buffer temperature. The relatively low thermal conductivities associated with polymeric microfluidic substrates (such as PDMS) make the rejection of this heat more difficult. In this paper, a combined experimental and numerical approach was used to examine Joule heating and heat transfer at a microfluidic intersection for PDMS/PDMS and PDMS/Glass hybrid systems.

In general the numerical and experimental thermal profiles were generally in agreement within ±3 °C, and, as expected, large temperature gradients were observed at the T intersection. Using these results it was found that the PDMS/Glass microfluidic systems maintained a much more uniform and lower buffer temperature than the PDMS/PDMS systems (a 500% increase in the buffer temperature was observed in some cases). Using the detailed 3D numerical model it was found that the majority of the heat is transferred from the microfluidic system through the lower substrate to the room temperature reservoir (as opposed to through the upper substrate), which the higher thermal conductivity of the glass substrate was more efficient at accomplishing. A simple steady state analysis was presented which revealed how this could be exploited to enhance heat transfer from these devices. In general the analysis revealed that a thinner lower substrate can significantly improve heat rejection, while the thickness of the upper substrate had a much smaller effect. This increase in temperature was shown to significantly increase the current load and doubled the volume flow rate through the PDMS/PDMS system. The flow structure and velocity profile remained relatively constant, despite the large temperature gradients, due to the counterbalancing effects of the decreased viscosity and decreased potential field gradient in the hotter sections of the channel. In general it was observed that (except in extreme cases) the channel aspect ratio had only a marginal effect on the temperature rise in the fluid system.
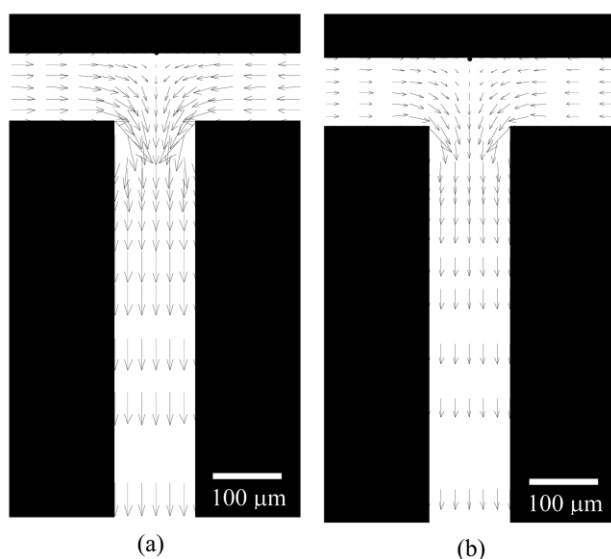
Acknowledgements

Fig. 10 Computed velocity vectors at the channel midplane in (a) PDMS/PDMS system and (b) PDMS/Glass systems 30s after 2.05kV potential field has been applied. Conditions are identical to those discussed for the experiments shown in Figs 3 and 4.
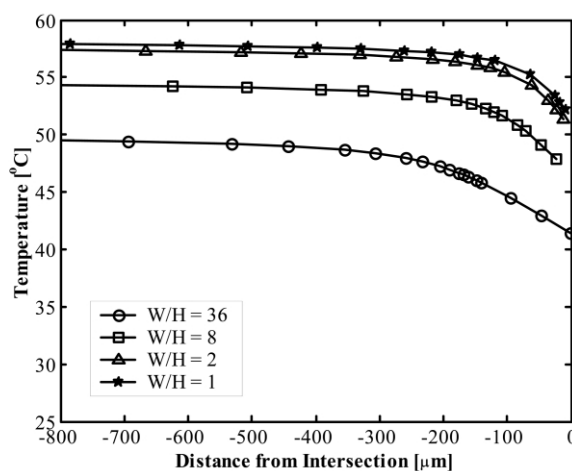

Fig. 11 Influence of channel aspect ratio on temperature profile in the mixing channel of a PDMS/PDMS system 30 s after a 2.05 kV voltage is applied. All channels have an equivalent cross sectional area of 3600 μm^2. W/H is the ratio of the mixing channel width to the mixing channel height.

References

1 T. Chovan and A. Guttman, *Trends Biotech.*, 2002, **20(3)**, 116–122.

2 S. C. Jakeway, A. J. de Mello and E. L. Russell, *Fresnius J. Anal. Chem.*, 2000, **366**, 525–539.

3 D. R. Reyes, D. Iossifidis, P.-A. Auroux and A. Manz, *Anal. Chem.*, 2002, **74**, 2623–2636.

4 J. Cheng and L. J. Kricka, *Biochip Technology*, Harwood Academic Publishers, Philadelphia, 2001.

5 M. Kock, A. Evans and A. Brunnschweiler, *Microfluidic Technology and Applications*; Research Studies Press, Hertfordshire, UK, 2000.

6 J. H. Knox and K. A. McCormack, *Chromatographia*, 1994, **38(3)**, 207–214.

7 J. H. Knox and K. A. McCormack, *Chromatographia*, 1994, **38(3)**, 215–221.

8 D. Erickson, D. Li and U. J. Krull, *Anal. Biochem.*, 2003, **317**, 186–200.

9 J. M. K. Ng, I. Gitlin, A. D. Stroock and G. M. Whitesides, *Electrophoresis*, 2002, **23**, 3461–3473.

10 J. C. McDonald and G. M. Whitesides, *Acc. Chem. Res.*, 2002, **35(7)**, 491–499.

11 M. L. Chabinyc, D. T. Chiu, J. C. McDonald, A. D. Stroock, J. F. Christian, A. M. Karger and G. M. Whitesides, *Anal. Chem.*, 2001, **73**, 4491–4498.

12 E. Delamarche, A. Bernard, H. Schmid, B. Michel and H. Biebuyck, *Science*, 1997, **276**, 779–781.

13 R. D. Johnson, I. H. A. Badr, G. Barrett, S. Lai, Y. Lu, M. J. Madou and L. G. Bachas, *Anal. Chem.*, 2001, **73**, 3940–3946.

14 G. B. Lee, S. H. Chen, G. R. Huang, W. C. Sung and Y. H. Lin, *Sens. Actuators B*, 2001, **75**, 142–148.

15 D. L. Pugmire, E. A. Waddell, R. Haasch, M. J. Tarlov and L. E. Locascio, *Anal. Chem.*, 2002, **74**, 871–878.

16 H. Becker and L. E. Locascio, *Talanta*, 2002, **56**, 267–287.

17 Y. Liu, J. C. Fanguy, J. M. Bledsoe and C. S. Henry, *Anal. Chem.*, 2000, **72**, 5939–5944.

18 S. L. R. Barker, D. Ross, M. J. Tarlov, M. Gaitan and L. E. Locascio, *Anal. Chem.*, 2000, **72**, 5925–5929.

19 D. C. Duffy, J. C. McDonald, O. J. A. Schueller and G. M. Whitesides, *Anal. Chem.*, 1998, **70**, 4974–4984. ⋆ *This work details the rapid prototyping technique used here for making PDMS based microfluidic systems.*

20 D. Ross, M. Gaitan and L. E. Locascio, *Anal. Chem.*, 2001, **73**, 4119–4123. ⋆⋆ *This paper was the first to describe the use of Rhodamine B as a temperature probe in microfluidic systems.*

21 M. E. Lacey, A. G. Webb and J. V. Sweedler, *Anal. Chem.*, 2000, **72**, 4991–4998.

22 K. L. Davis, K. L. K. Liu, M. Lanan and M. D. Morris, *Anal. Chem.*, 1994, **66**, 3744–3750.

23 K. Swinney and D. J. Bornhop, *Electrophoresis*, 2002, **23**, 613–620.

24 A. M. Chaudhari, T. M. Woudenberg, M. Albin and K. E. Goodson, *J. MEMS*, 1998, **7(4)**, 345–355.

25 H. Mao, T. Yang and P. S. Cremer, *J. Am. Chem. Soc.*, 2002, **124**, 4432–4435.

26 J. Lou, T. M. Finegan, P. Mohsen, T. A. Hatton and P. E. Laibinis, *Rev. Anal. Chem.*, 1999, **18**, 235–284.

27 D. Ross and L. E. Locascio, *Anal. Chem.*, 2002, **74**, 2556–2564.

28 J. Sakakibara and R. J. Adrian, *Exp. Fluids*, 1999, **26**, 7–15.

29 R. M. Guijt, A. Dodge, G. W. K. van Dedem, N. F. de Rooij and E. Verpoorte, *Lab Chip*, 2003, **3**, 1–4.

30 S. V. Ermakov, S. C. Jacobson and J. M. Ramsey, *Anal. Chem.*, 1998, **70**, 4494–4504.

31 F. Bianchi, R. Ferrigno and H. H. Girault, *Anal. Chem.*, 2000, **72**, 1987–1993.

32 N. A. Patankar and H. H. Hu, *Anal. Chem.*, 1998, **70**, 1870–1881.

33 J. I. Molho, A. E. Herr, B. P. Mosier, J. G. Santiago, T. W. Kenny, R. A. Brennen, G. B. Gordon and B. Mohammadi, *Anal. Chem.*, 2001, **73**, 1350–1360.

34 S. K. Griffiths and R. H. Nilson, *Anal. Chem.*, 2000, **72**, 5473–5482.

35 D. Erickson and D. Li, *Langmuir*, 2002, **18**, 1883–1892. ⋆ *This work provides the details for the fluidic version of the 3D numerical code used here.*

36 L. Jiang, J. Mikkelsen, J. M. Koo, D. Huber, S. Yao, L. Zhang, P. Zhou, J. G. Maveety, R. Prasher, J. G. Santiago, T. W. Kenny and K. E. Goodson, *IEEE Trans. Components Packaging Tech.*, 2002, **25(3)**, 347–355.

37 D. Maynes and B. W. Webb, *Int. J. Heat Mass Transfer*, 2003, **46(8)**, 1359–1369.

38 T. S. Zhao and Q. Liao, *J. Micromech. Microeng.*, 2002, **12**, 962–970.

39 M. Jansson, A. Emmer and J. Roeraade, *J. High Resolut. Chromatogr.*, 1989, **12**, 797–801.

40 F. P. Incropera and D. P. DeWitt, *Introduction to Heat Transfer*, John Wiley & Sons: New York, 1996.

41 R. L. Panton, *Incompressible Flow*, John Wiley & Sons: New York, 1996.

42 D. Ross, T. J. Johnson and L. E. Locascio, *Anal. Chem.*, 2001, **73**, 2509–2515.

43 F. M. White, *Fluid Mechanics*; McGraw-Hill: New York, 1994.

44 X. Ren, M. Bachman, C. Sims, G. P. Li and N. Allbritton, *J. Chromatogr., B*, 2001, **762**, 117–125.

45 Thermophysical properties of Sylgard 184 Poly(dimethylsiloxane) obtained from manufacturers "Product Information" and through personal communications.

46 R. L. Chien, *Electrophoresis*, 2003, **24(3)**, 486–497.

47 M. Urbanek, L. Krivankova and P. Bocek, *Electrophoresis*, 2003, **24(3)**, 466–485.